REPORT DOCUMENTATION PAGE

Form Approved
OMB No. 0704-0188

1. REPORT DATE (DD-MM-YYYY)	2. REPORT TYPE	3. DATES COVERED (From - To)
06-04-2002	Journal Article	Jun 2001 - Apr 2002

4. TITLE AND SUBTITLE
Investigation of the State-to-State Rotational Relaxation Rate Constants for Carbonmonoxide (CO) Using Infrared Double Resonance

5a. CONTRACT NUMBER
In-house

5b. GRANT NUMBER

5c. PROGRAM ELEMENT NUMBER

6. AUTHOR(S)
Steve P. Phipps, Tony C. Smith and Gordon D. Hager (1)
Michael C. Heaven (2)
J.K. McIver and W.G. Rudolph (3)

5d. PROJECT NUMBER
4866

5e. TASK NUMBER
LB

5f. WORK UNIT NUMBER
07

7. PERFORMING ORGANIZATION NAME(S) AND ADDRESS(ES)

1)Air Force Research Laboratory/Directed Energy Directorate,Kirtland Air Force Base, New Mexico 87117-5776
2)Department of Chemistry, Emory University, Atlanta, Georgia 30322
3)Department of Physics and Astronomy, University of New Mexico, Albuquerque, New Mexico 87131-3031

8. PERFORMING ORGANIZATION REPORT NUMBER

9. SPONSORING / MONITORING AGENCY NAME(S) AND ADDRESS(ES)
Air Force Research Laboratory/Directed Energy Directorate,Kirtland Air Force Base, New Mexico 87117-5776

10. SPONSOR/MONITOR'S ACRONYM(S)

11. SPONSOR/MONITOR'S REPORT NUMBER(S)

12. DISTRIBUTION / AVAILABILITY STATEMENT
Approved for public release; distribution is unlimited

13. SUPPLEMENTARY NOTES
Article citation: J. Chem. Phys., **116**, 9281-9292 (2002)

14. ABSTRACT
State-to-state rotational relaxation of carbon monoxide (CO) has been studied using an IR double resonance technique. Individual rotational lines of the (2-0) vibrational overtone band were pumped by a pulsed tunable IR laser and the subsequent evolution of the v=2 rotational population distribution was monitored by the absorption of a tunable cw IR laser via the (3-2) band transitions. Both the excitation and probe lasers were linearly polarized, with linewidths that were narrower than the CO Doppler width. Consequently, alignment and velocity relaxation effects were observed in these measurements. A data set consisting of 54 time-dependent rotational state population profiles was acquired. The full CO-CO rotational relaxation matrix, which consists of state-to-state rate constants for rotational levels up to J = 29, was deduced from computer simulations of the data. Scaling and fitting laws were used to provide parametric representations of the rate constants. The three most common models, modified exponential gap (MEG), statistical polynomial-exponential gap (SPEG), and energy corrected sudden with exponential-power gap (ECS-EP) were investigated. We concluded that the SPEG law best reproduced the CO-CO rotational energy transfer data. A propensity to preserve the CO parity in rotational energy transfer was observed for collisions where the amount of energy transferred was small. Hence, even ΔJ processes were favored for transitions between levels with low J values. For near-single collision events a correlation was noted between the amount of rotational energy transferred and the degree of velocity distribution relaxation. This correlation yielded insights regarding the energy transfer dynamics.

15. SUBJECT TERMS
IR-IR double resonance, CO+CO

16. SECURITY CLASSIFICATION OF:			17. LIMITATION OF ABSTRACT	18. NUMBER OF PAGES	19a. NAME OF RESPONSIBLE PERSON
a. REPORT	b. ABSTRACT	c. THIS PAGE			David A. Hostutler
unclassified	unclassified	unclassified	Unlimited	12	19b. TELEPHONE NUMBER (include area code) 505-853-2680

Investigation of the state-to-state rotational relaxation rate constants for carbon monoxide (CO) using infrared double resonance

Steve P. Phipps, Tony C. Smith, and Gordon D. Hager[a)]
Air Force Research Laboratory/Directed Energy Directorate, Kirtland Air Force Base, New Mexico 87117-5776

Michael C. Heaven
Department of Chemistry, Emory University, Atlanta, Georgia 30322

J. K. McIver and W. G. Rudolph
Department of Physics and Astronomy, University of New Mexico, Albuquerque, New Mexico 87131-3031

(Received 30 January 2002; accepted 5 March 2002)

State-to-state rotational relaxation of carbon monoxide (CO) has been studied using an ir double resonance technique. Individual rotational lines of the (2-0) vibrational overtone band were pumped by a pulsed tunable ir laser and the subsequent evolution of the $v=2$ rotational population distribution was monitored by the absorption of a tunable cw ir laser via the (3-2) band transitions. Both the excitation and probe lasers were linearly polarized, with linewidths that were narrower than the CO Doppler width. Consequently, alignment and velocity relaxation effects were observed in these measurements. A data set consisting of 54 time-dependent rotational state population profiles was acquired. The full CO–CO rotational relaxation matrix, which consists of state-to-state rate constants for rotational levels up to $J=29$, was deduced from computer simulations of the data. Scaling and fitting laws were used to provide parametric representations of the rate constants. The three most common models, modified exponential gap, statistical polynomial-exponential gap (SPEG), and energy corrected sudden with exponential-power gap (ECS-EP) were investigated. We concluded that the SPEG law best reproduced the CO–CO rotational energy transfer data. A propensity to preserve the CO parity in rotational energy transfer was observed for collisions where the amount of energy transferred was small. Hence even ΔJ processes were favored for transitions between levels with low J values. For near-single collisions events a correlation was noted between the amount of rotational energy transferred and the degree of velocity distribution relaxation. This correlation yielded insights regarding the energy transfer dynamics. © *2002 American Institute of Physics.* [DOI: 10.1063/1.1472516]

I. INTRODUCTION

Rotational energy transfer (RET) rates influence many fundamental processes such as sound propagation, absorption, and dispersion in a gas medium,[1–4] the population evolution of nonequilibrium systems like the high temperature environment of flames,[4,5] the viscosity of a gas,[4] optical pumping processes,[6–11] and the pressure broadening of spectral linewidths.[12–14] Data for RET processes are needed to predict and explain the final quantum state populations of exothermic reactions[15–17] and chemical lasers.[18,19] RET can increase the efficiency of an optically pumped molecular laser (OPML) by decreasing saturation of the pump transition. This is accomplished by removing population from the upper populated level while simultaneously adding population to the lower depleted level. Efficient RET in CO+CO collisions has been invoked to explain the high efficiency of (2-0) band pumping of a CO OPML,[20] while transfer of population out of the pumped rotational level to adjacent levels results in multiline lasing on the (2-1) band.[21] It has been shown that the CO OPML can operate single frequency and is tunable between 4.63 and 4.88 μm using a diffraction grating to select various R- and P-branch transitions of the (2-1) band.[21]

Initial efforts to determine the RET rate constants for CO focused on thermal conductivity and speed of sound measurements.[22–25] More recently, rotational relaxation rate constants of CO have been deduced from free jet expansion data by measuring the extent to which rotational populations reach equilibrium before collisions in the freely expanding gas diminish.[26–30] However, since these methods are not state resolved they are insensitive to the details of the state-to-state rate constant matrix. For CO the most common methods employed for the study of RET rate constants have focused on spectral properties, such as linewidth measurements of Raman Q-branch transitions.[13,14,31] The linewidths define the rate at which a specific rotational level experiences phase-interrupting collisions, but they do not provide information about the range of final states populated. Interpretation of this data is further complicated by the fact that the linewidths are determined by contributions from both inelastic (rotational and vibrational relaxation) and elastic (pure dephasing) collisional processes.

Although infrared (ir) double resonance experiments

a)Author to whom correspondence should be addressed; electronic mail: gordon.hager@kirtland.af.mil

provide the most accurate and sensitive method to make direct observations of state-to-state transfer processes, the technical challenge they pose is such that only two ir pump-probe experiments have been reported for CO.[32,33] In these studies rotational relaxation of CO was examined using a pulsed CO laser to populate a single rotational level of $v=1$, while a cw CO laser was used to monitor the time-dependent evolution of the population in adjacent rotational levels, via the (2-1) band absorption. State-resolved transfer processes were characterized, but the group of rotational levels investigated was too small to permit the construction of a complete rate constant matrix. At present, there is considerable disagreement between the sets of RET rate constants reported by previous investigators.

Our studies of CO+CO RET are motivated, in part, by ongoing efforts to develop CO overtone lasers. In addition, CO RET is of relevance to processes occurring in the atmosphere, interstellar space, and hydrocarbon combustion. From a theoretical perspective it is of interest to learn which of the most common forms of rate constant scaling relationships best represent CO RET data. In the present work we have considered the modified exponential gap (MEG),[14,34] statistical polynomial-exponential gap (SPEG),[14,35,36] and energy corrected sudden with exponential-power gap (ECS-EP)[12,37,38] models. Looney *et al.*[14] suggested that CO RET has a tendency to conserve parity, and we have been able to quantify this effect. Lastly, as the CO+CO system is computationally tractable, the data obtained in this study will be suitable for testing high-level theoretical models of diatom–diatom scattering processes.

In this paper we present the most extensive investigation to date of the room temperature CO–CO RET. The rate constant matrix ($J=0-29$) was deduced from a data set that consisted of population evolutions for 54 different pump and probe transition combinations. The MEG, SPEG, ECS-EP scaling laws were used to generate rotational relaxation rate constant matrices. Time-dependent level populations were simulated by numerical solution of the master equation. Computed temporal profiles were compared with the experimental results to determine which of the scaling relationships gave the most realistic results.

Correlations between the quantity of rotational energy transferred and the extent of velocity randomization were noted during these measurements. These correlations revealed aspects of the energy transfer process that are readily appreciated using classical models.

II. EXPERIMENT

An energy level diagram that illustrates the pump-probe transition scheme used in the CO double resonance experiment is shown in Fig. 1. The long solid arrow represents the pump laser wavelength that was tuned to a selected transition of the (2-0) overtone band of CO that prepared a single rotational level in $v=2$. The probe laser was then tuned to various transitions of the (3-2) band and its time-resolved transmittance was monitored to follow the rotational populations in the pumped and adjacent rotational levels. The short solid arrow in Fig. 1 represents a (3-2) band probe transition from the rovibrational level that was directly populated by the pump laser. The dashed arrows represent probe transitions that originate from rotational levels that were populated by RET.

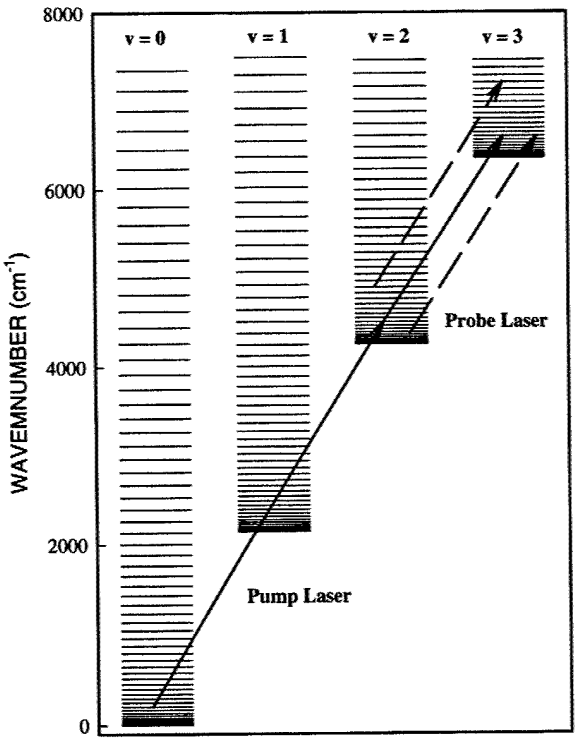

FIG. 1. An energy level diagram which illustrates the pump-probe transition scheme used in the CO ir double resonance experiment.

The apparatus used for these measurements is shown in Fig. 2. CO gas was contained in a stainless steel absorption cell. The cell was a 71 cm long tube with a clear aperture of 6 cm diameter. It was fitted with a gas inlet/outlet valve and wedged calcium fluoride (CaF_2) windows. The CO gas pressure and temperature inside the absorption cell were measured by a capacitance manometer (MKS, Baratron 622A02TBE) and a *K*-type thermocouple, respectively. Typical conditions were $P=2$ Torr and $T=297$ K. Frequently during the experiment, the gas inside the absorption cell was

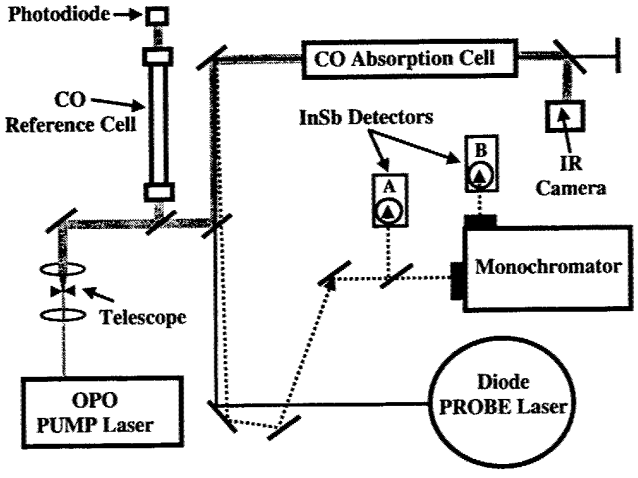

FIG. 2. A schematic diagram of the pump-probe experimental apparatus.

evacuated and replaced with fresh CO (Air Products, ultra-high purity) to ensure that the purity remained high.

The pump laser was a narrow bandwidth (~165 MHz) pulsed tunable optical parametric oscillator (OPO) system operating at 10 Hz with a temporal pulse width of 6 ns. The OPO system has been described in detail elsewhere[20,21] and therefore only a short description will be given here. The energy source for the OPO was an injection-seeded Nd:YAG laser (Spectra-Physics, GCR 170-10) that operated on a single longitudinal cavity mode and used second harmonic generation to efficiently produce an output wavelength of 532 nm. The OPO was seeded with radiation from a temperature stabilized cw diode laser (New Focus, 6203) which was tuneable between 680 and 693 nm while having a bandwidth less than 5 MHz and an output power ~5 mW. The OPO output could be tuned from 2.29 to 2.44 μm, with an output power of ~4 mJ per pulse.

In the first experiments it was found that, if the gain in the CO gas cell produced by the pump laser pulse was sufficiently high, undesirable amplified spontaneous emission (ASE) would result. To reduce the single pass gain through the absorption cell a Keplarean telescope was used to expand the diameter of the pump beam from 3.4 to 26.5 mm. The pump beam power was further attenuated by placing a 0.635 mm diameter pinhole at the focus of the telescope. This reduced the output power by a factor of 10 and greatly enhanced the beam quality. An ir camera (Spiricon, Pyrocam I) was used to view the pump beam after it had passed through the CO cell (see Fig. 2). This camera monitored the spatial profile of the pump beam during the experiments and was used to check that the pump beam was aligned through the center of the absorption cell.

To ensure that the pump radiation was at least near resonant with the desired CO transition the ir wavelength of the OPO was determined indirectly by measuring the frequency of the cw seed diode beam with a wavemeter (Burleigh, WA-20). Once the ir frequency had been determined by this method, only minor adjustments were needed to tune the pump into resonance with the CO transition of interest. Fine-tuning was guided by observing the transmittance of a small portion of the pump beam through a reference cell that contained 30 Torr of CO. A sharp decrease in the transmission through the reference cell was seen as the OPO was tuned into resonance. It was essential that the OPO pump laser provided a stable, fixed-frequency output over the duration of each temporal profile measurement. Hence the transmission through the reference cell was monitored to ensure that there was no significant frequency drift during the data acquisition period. Measurements were terminated whenever frequency drift was detected.

The probe laser was a narrow bandwidth (~30 MHz) cw lead salt diode laser (Muetek, GMBH OLS-150) tunable between 4.6 and 5.0 μm with an output power of ~1.0 mW. The probe beam passed twice through the CO absorption cell, with the return beam slightly off-axis relative to the incoming beam, as represented by the dashed line in Fig. 2. The transmittance of the probe beam was monitored with two liquid nitrogen cooled InSb detectors (Kolmer Technologies, KISDP-0.5-J1, 10 ns rise time and a 12 kV/W sensitivity). Since the InSb detectors were sensitive to both the pump and probe laser wavelengths, long pass filters where placed in front of the detectors to absorb the pump radiation. The wavelength of the probe laser was tuned by changing the temperature and current across the liquid nitrogen cooled laser diode. Inconveniently, the current and temperature settings needed to bring the diode laser frequency into resonance with a desired CO transition were found to change daily. To confirm that the probe laser was resonant with the CO transition of interest, the wavelength of the probe laser was measured using a 0.3 m monochromator (McPherson, 218 with a 150 lines/mm grating blazed at 4.0 μm).

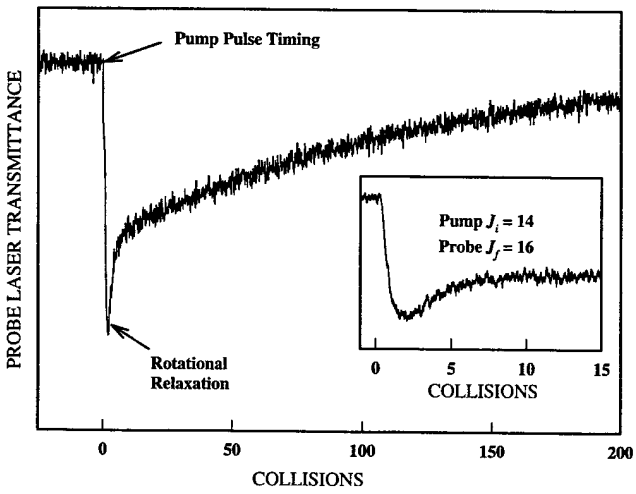

FIG. 3. A pump-probe infrared double resonance signal which displays the collision-dependant transmittance of the probe laser that was tuned to the $R(16)$ transition of the (3-2) band of CO. A sharp decrease occurs in the cw probe transmittance after the pulsed pump laser timing which was tuned to the $R(13)$ transition of the (2-0) overtone band. The double resonance signal displays rapid rotational relaxation at early collisions while vibrational loss from $v=2$ is responsible for the long exponential decay. The inset is an expanded region of the double resonance signal and shows that the CO–CO rotational relaxation process is complete by ~7 CO hard sphere collisions.

As linearly polarized lasers were used in these experiments care was taken to make sure that the results were not influenced by effects related to the relaxation of an initially aligned population. These complications were avoided by recording the double resonance data with the pump and probe laser polarizations set at the magic angle (54.74°).

III. RESULTS

A typical pump-probe ir double resonance signal is displayed in Fig. 3. For this trace the pump laser was tuned to the $R(13)$ line of the (2-0) overtone band while the probe laser was tuned to the $R(16)$ transition of the (3-2) band. The abscissa of Fig. 3 is labeled using both time and the CO–CO hard sphere collision number ($x=k_{HS}[CO]t$). The latter was calculated with the assumption that the hard sphere collision diameter is 4.0 Å,[39] which gives a collision rate constant of $k_{HS}=3.4\times10^{-10}$ cm^3 s^{-1}. The advantage of using the collision number scale is that it facilitates the comparison of data recorded at different pressures.

As the vibrational frequency of CO is quite high ($\omega_e=2170$ cm^{-1})[40] the room temperature thermal population in $v=2$ is negligible. Consequently, prior to the pump pulse the

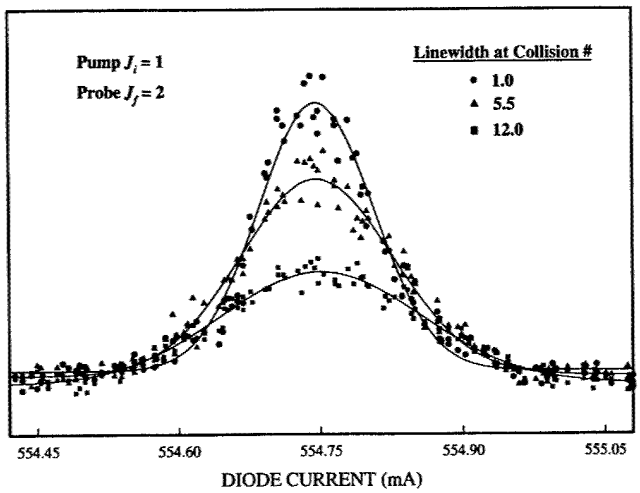

FIG. 4. The figure displays the collision-dependent evolution of the $P(2)$ lineshape following excitation of $J_i=1$. Since the pump laser had a sub-Doppler linewidth the probe laser absorption had to be corrected for the effects of velocity relaxation. Linewidths were extracted by fitting Gaussian functions to the frequency-resolved data which are represented by the solid lines.

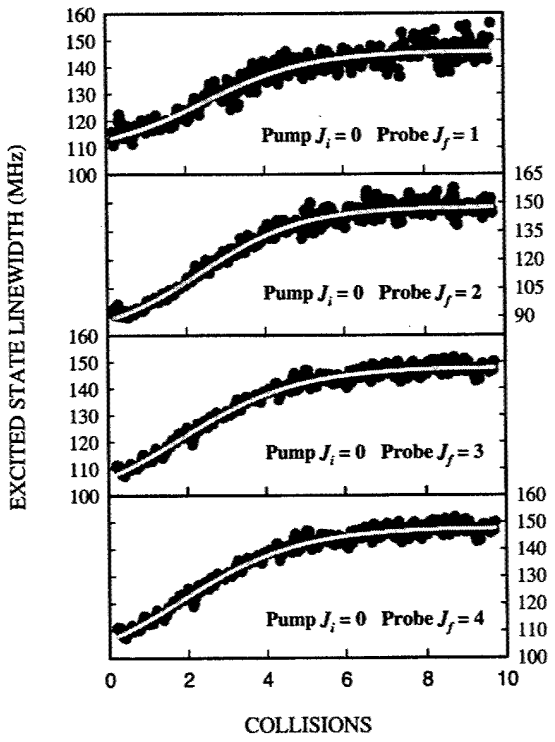

FIG. 5. Experimentally determined collision-dependent excited state linewidths (in MHz) for the $J_f=1$, 2, 3, and 4 levels following excitation of $J_i=0$. The experimental data is represented by dots while the line through the center of the data is a fit of the collision-dependent linewidths using the function in Eq. (1).

transmittance of the probe laser beam through the CO absorption cell is near 100%, as represented by the baseline in the double resonance signal (see Fig. 3). The pump laser pulse produced a near instantaneous population in $J=14$ of $v=2$ and collisions rapidly redistributed this population among the neighboring rotational levels. The rapid growth of population in $J=16$ is visible as a sharp decrease in the probe transmittance immediately following the pump laser pulse. Although the transfer is fast, it clearly imparts a measurable rise time to the signal. This is illustrated by the inset in Fig. 3, where it can be seen that the $J=16$ population reaches a maximum after just two hard sphere collisions. The double resonance signal contains information about both rotational and vibrational relaxation. RET is so rapid that it is complete within approximately seven hard sphere collisions (see below). The slow decay evident in Fig. 3 from about 15 to 200 collisions is caused by vibrational relaxation.

The effects of velocity changing collisions were readily observed in these experiments. The pump laser linewidth (~165 MHz) was narrower than the 300 MHz Doppler width (297 K) of the CO lines occurring near 2.35 μm. Consequently, the pump laser excited a velocity subgroup such that frequency scans of the probe laser over lines that originated from the pumped level revealed a sub-Doppler linewidth. For low collision numbers the levels populated by collisions also exhibited sub-Doppler linewidths, although these were broader than the lineshape of the initially populated level. These results showed that velocity changing collisions and RET were occurring with comparable rate constants. This circumstance complicated the process of recording and analyzing the time-resolved absorption data. As the lineshape changed with time it was not sufficient to monitor the population of a given level by observing the absorption at the line center. As the area under the absorption line is proportional to the population, it would seem reasonable to record frequency scans of the probe laser over the absorption lines for a range of pump-probe delay times. The populations could then be recovered from the integrated intensity data. Unfortunately, the data acquisition time for this approach places unreasonable demands on the stability of the lasers.

To overcome this problem the data acquisition was performed in two stages. First the time-dependent absorption signal for each probe transition was recorded with the probe laser tuned to the line center. Then the lineshape for each transition was recorded for a range of delay times. Linewidths were extracted by fitting Gaussian functions to the frequency-resolved data. For example, Fig. 4 shows the evolution of the $P(2)$ lineshape following excitation of $J=1$. Plots of the linewidths of transitions from the $J=1$, 2, 3, and 4 levels, populated after excitation of $J=0$, are shown in Fig. 5. The sigmoid shape of these plots is typical of all of the linewidth versus collision number data. Time- and frequency-resolved data sets were recorded using $J=0$, 7, and 14 as the initially pumped levels. These levels were chosen as they sample the 300 K Boltzmann rotational distribution below, at, and above the maximum. All final states in the range $J=0-18$ were examined, with the exception of $J=15$. The latter could not be characterized as the probe laser would not operate at the frequencies that are resonant with the $P(15)$ or $R(15)$ lines.

A. Data reduction

To separate RET from the effects of vibrational relaxation and velocity changing collisions, corrections were applied to the time-dependent absorption curves. As the absorp-

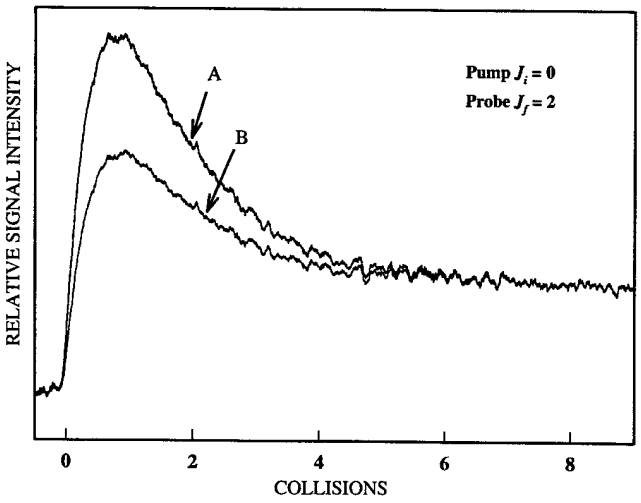

FIG. 6. The figure displays collision-dependent population evolutions for $J_f=2$ after excitation of $J_i=0$. The upper trace A and lower trace B represent a population evolution before and after being corrected for velocity relaxation, respectively.

tion measurements were made with the probe laser tuned to the line center, it was necessary to adjust for the fact that the lines became broader with increasing numbers of collisions. The line center absorption data can be rendered proportional to the population by dividing by the linewidth. To perform this division it was convenient to represent the collision number dependent linewidths by parametric equations. The function

$$\Delta\upsilon(x)=a_1+\frac{b_1}{1+\exp[-(x-c_1)/d_1]} \tag{1}$$

was found to give a good representation of the linewidth data, where a_1, b_1, c_1, and d_1 are adjustable fitting parameters. (In the following the subscripts for the fitting parameters are chosen to coincide with the equation number.) Examples of the fitted curves are shown in Fig. 5. The correction for velocity relaxation was then applied as a scaling factor that was inversely proportional to the linewidth, such that

$$F(J_i,J_f,x)=f(J_i,J_f,x)\frac{\Delta\upsilon(x)}{\Delta\upsilon(0)}, \tag{2}$$

where $f(J_i,J_f,x)$ is the measured absorption profile for excitation of J_i and observation of J_f. Figure 6 illustrates the effect of applying the correction for velocity relaxation. The curves shown here are for initial excitation of $J_i=0$ and detection of the population in $J_f=2$. Traces A and B are the $f(0,2,x)$ and $F(0,2,x)$ functions, respectively. From this figure it is clear that the error incurred by ignoring the velocity relaxation would be severe.

The correction for vibrational relaxation was straightforward. The rate constant for vibrational loss[41] from $\upsilon=2$ is $k_\upsilon=2.73\times10^{-12}$ cm^3 s^{-1}. Rotational populations were monitored for delay times equivalent to about 15 collisions, by which time rotational equilibrium had been achieved. During this time 12% of the initial population was lost through vibrational relaxation. To correct the absorption curves for this loss it was assumed that the rate constants for vibrational relaxation were independent of the rotational level. Absorption curves corrected for vibrational relaxation could then be defined by

$$P(J_i,J_f,x)=F(J_i,J_f,x)\exp\left(\frac{k_\upsilon x}{k_{\mathrm{HS}}}\right), \tag{3}$$

where k_{HS} is the rate constant for CO–CO hard sphere collisions.

The corrections described so far provided curves that reflected the change in the population of a given level as the number of collisions increases, but the relative amplitudes of the $P(J_i,J_f,x)$ curves for different values of J_i and J_f were not meaningful. To generate a set of related curves we took advantage of the fact that the rotational distributions could be nearly thermalized within the typical upper collision number of the measurements. After about seven collisions the $P(J_i,J_f,x)$ curves became almost flat, indicating that near rotational equilibrium conditions had been achieved. To provide a way to represent the data, and a means to extrapolate to equilibrium conditions, the $P(J_i,J_f,x)$ curves were represented by the expression

$$\begin{aligned}\bar{P}(J_i,J_f,x)&=a_4\Bigg[1-\exp(-b_4x)-\frac{c_4}{c_4+d_4}\Bigg(1\\&\quad+\frac{b_4\exp[-(c_4+d_4)x]-(c_4+d_4)\exp(-b_4x)}{c_4+d_4-b_4}\Bigg)\Bigg],\end{aligned} \tag{4}$$

where a_4, b_4, c_4, and d_4 are fitting parameters. A two stage procedure was used to fit Eq. (4) to the $P(J_i,J_f,x)$ curves. First, each curve was fit independently to define the parameters that control the shape of the curve (b_4 through d_4). In the second step the a_4 values were scaled so that the rotational equilibrium population was recovered for large values of x. Examples of the fitted curves for $J_i=0$ and $J_f=0$, 1, 2, 3, and 4 are shown in Fig. 7. The full set of parameters for all of the curves recorded in this study is presented in Table I.

For the initially excited level the rise time of the $f(J_i,J_i,x)$ curve was very fast, and the probe signal reached a maximum within 20 ns. The InSb detector/preamplifier combination was not fast enough to respond linearly to this signal, so the $J_f=J_i$ curves suffered from instrumental distortion immediately following the excitation pulse. Because of this problem, fits to the $J_f=J_i$ data that were constrained to yield an equilibrium population at large x did not give a good fit to the low x region of the curve. This deficiency is evident in the first panel of Fig. 7. As this problem originated from an instrumental artifact we did not impose any further corrections on the data.

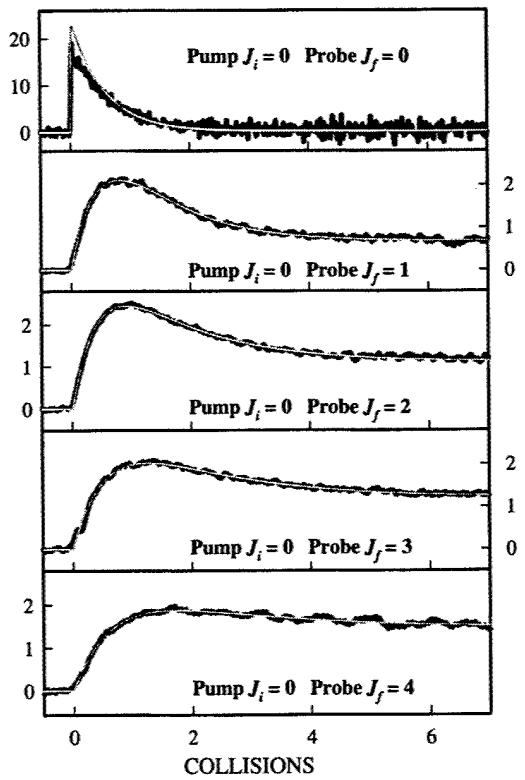

FIG. 7. The collision-dependent rotational population evolutions for $J_f = 0$, 1, 2, 3, and 4 after excitation of $J_i = 0$. The fit to the data is represented by the line through the center of the rotational populations using the parametric Eq. (4).

B. Definition of the master equation using scaling and fitting laws

Once vibrational relaxation has been factored out, the evolution of the rotational population within the $v = 2$ manifold is described by the set of coupled differential equations (the master equation) given by

$$\frac{dN_J}{dt} = \sum_{J'} (k_{J \leftarrow J'} N_{J'} - k_{J' \leftarrow J} N_J)[\mathrm{CO}], \tag{5}$$

where N_J is the population of the Jth level (in number density units) and $k_{J \leftarrow J'}$ is the rate constant for transfer from level J' to J. In principle the summation in Eq. (5) runs over all possible rotational levels, but in practice it is sufficient to consider the subset of levels that have significant thermal populations. At 300 K more than 97% of the population of CO $v = 2$ resides in levels with $J < 20$. To solve the equations for this set of levels we need a matrix of 400 state-to-state rate constants. Applying detailed balance and setting the diagonal elements to zero reduces the number of independent rate constants to 190, but this is still too many parameters to be determined from the data acquired in these experiments. Consequently, we have adopted the usual strategy of generating families of rate constants from scaling and fitting laws. The laws that have been examined were derived from atom–molecule scattering formalisms. This approach is reasonable as the present measurements do not yield information concerning state changes of the collision partner. The observed transfer events were averaged over all rotational levels of ground state CO. This averaging has the effect of making the CO induced transfer behave as if the collision partner is spherically symmetric. Note that atom–molecule scattering models have been used successfully to treat diatom–diatom collisions in previous studies.

Three different models were used to generate the state-to-state rate constants. The first two were based on heuristic fitting law expressions. Previous investigators have used the modified energy gap (MEG) law and the statistical exponential-power gap (SPEG) law to analyze CO–CO RET data. In the present work we used the MEG law in the form

$$k^{\mathrm{MEG}}_{J' \leftarrow J} = \alpha_6 \left(\frac{1 + a_6 E(J)/c_6 kT}{1 + a_6 E(J)/kT} \right)^2 \exp\left(\frac{-b_6 \Delta E_{J'J}}{kT} \right) \tag{6}$$

TABLE I. Coefficients for Eq. (4) which represent the collision-dependent rotational relaxation populations.

Probe	Pump $J_i = 0$				Pump $J_i = 7$				Pump $J_i = 14$			
J_f	a[a]	b_4	c_4	d_4	a_4	b_4	c_4	d_4	a_4	b_4	c_4	d_4
0	21.672	150	1.7801	0.0162	0.428	0.9102	0.1708	0.5486	0.375	0.3662	8.8307	20.6670
1	3.468	1.8143	0.9165	0.1824	1.472	0.6584	0.2169	0.4087	1.361	0.4600	8.9400	11.8000
2	3.033	2.3048	0.5009	0.2198	2.029	0.8968	0.1179	0.3759	1.689	0.4270	5.7200	16.0000
3	2.956	1.7657	0.3465	0.2452	3.486	0.6773	0.3207	0.4542	1.853	0.4320	3.4100	27.3000
4	7.971	0.4761	1.2856	0.2889	3.108	1.1320	0.0995	0.3665	2.019	0.4620	1.3500	52.7000
5	2.255	1.3803	0.1115	0.2907	2.990	1.9705	0.0183	0.1741	2.474	0.4740	3.8000	29.9000
6	3.054	0.7907	0.3013	0.3929	3.146	1.8918	0.0284	0.3124	2.526	0.5170	3.0600	35.0000
7	2.647	0.6611	0.2127	0.4178	35.780	150	1.15	0.1025	4.420	0.5280	3.5300	4.0300
8	2.620	0.5418	0.2049	0.3889	3.385	1.5899	0.0974	0.5358	10.785	0.1460	0.5690	0.1550
9	2.819	0.3851	0.2646	0.3612	3.695	0.9116	0.2446	0.6755	10.627	0.1670	0.7000	0.1810
10	2.039	0.4381	0.1287	0.3539	5.020	0.5713	0.7061	0.6977	23.894	0.1060	1.2600	0.1160
11	1.774	0.4168	0.1114	0.3432	4.801	0.4922	0.7258	0.6310	2.740	0.9500	0.3320	0.6320
12	1.782	0.3090	0.1347	0.2538	4.490	0.3170	0.5146	0.3960	2.974	1.2600	0.3540	0.3930
13	1.613	0.2380	0.1069	0.1600	3.670	0.5077	3.4864	2.8660	2.637	1.5900	0.2950	0.3010
14	3.406	0.3651	10.1914	3.2977	3.468	0.2197	0.3998	0.2680	29.730	160	1.09	0.0421
15	[b]											
16	0.994	0.1965	0.1761	0.2104	1.726	0.3932	5.8482	6.2022	5.003	0.4730	1.3200	0.2190
17	1.251	0.1100	0.2247	0.1157	1.890	0.3237	8.8616	5.1436	1.753	0.6000	0.5660	0.2610
18	1.173	0.0814	0.2148	0.0802	1.543	0.3213	10.5115	5.4570	1.021	0.6090	0.3780	0.2640

[a]Parameter has unit of number density as (10^{11} molecules cm^{-3}); sufficient digits are quoted to reproduce the original data to full accuracy.
[b]Probe transitions from $J_f = 15$ were not observed due to a gap in the laser tuning region.

for upward ($J'>J$) energy transfer. In Eq. (6), α_6, b_6, and c_6 are fitting parameters, and $\Delta E_{J'J}$ is the magnitude of the energy gap, $|E(J')-E(J)|$. The a_6 parameter reflects the duration of the collision. To be consistent with earlier studies we have adopted the value $a_6=2$. The version of the SPEG relation used here was defined by

$$k^{\mathrm{SPEG}}_{J'\leftarrow J}=\alpha_7\left(\frac{\Delta E_{J'J}}{B_{v=2}}\right)^{-c_7}\exp\left(\frac{-b_7\Delta E_{J'J}}{kT}\right) \tag{7}$$

for upward transfer, where $B_{v=2}$ is the CO rotational constant. Equations (6) and (7) implicitly assume that there is no change in the angular momentum projection quantum number ($\Delta M_J=0$) and that the density of transnational states is approximately unchanged by an RET event. Downward energy transfer rate constants were obtained by applying the principle of detailed balance such that

$$k^{\mathrm{MEG/SPEG}}_{J\leftarrow J'}=k^{\mathrm{MEG/SPEG}}_{J'\leftarrow J}\left(\frac{2J+1}{2J'+1}\right)\exp\left(\frac{\Delta E_{J'J}}{kT}\right). \tag{8}$$

The third model used to generate rate constants was the energy corrected sudden (ECS) scaling law. This model was developed from an approximate treatment of atom–diatom RET scattering dynamics. This formalism begins by assuming that the target molecule does not rotate during the collision [infinite order sudden (IOS) approximation]. For CO–CO collisions the molecule does undergo some rotation during the collision and the IOS approximation must be corrected accordingly. The energy corrected sudden (ECS) scaling law is a modification of the IOS model that takes into account rotation of the molecule during the collision. The rotational energy transfer rate constant matrix was generated from the ECS expression

$$k^{\mathrm{ECS}}_{J'\leftarrow J}=(2J'+1)\exp\left(\frac{E(J)-E(J_>)}{kT}\right)[\Omega_{J>}]^2 \times\sum_{\ell=|J'-J|}^{J'+J}\begin{bmatrix}J & J' & \ell\\ 0 & 0 & 0\end{bmatrix}^2[\Omega_{\ell>}]^{-2}(2\ell+1)k^{\mathrm{EP}}_{\ell\leftarrow 0}, \tag{9}$$

where $E(J_>)$ is the larger of $E(J)$ or $E(J')$, the term [:::] is a 3-J symbol,[42] and detailed balance was imposed by the first two factors. The $\Omega_{J>}$ term is the adiabatic factor that accounts for molecular rotation during the collision. In addition to the well-defined molecular parameters that determine $\Omega_{J>}$ this factor also depends on the CO–CO interaction length (l_c), which is treated as a variable fitting parameter. Equation (9) generates the full matrix of rate constants from a single basis vector defined by the $k_{\ell\leftarrow 0}$ values. These, in turn, have been derived from various parameterization schemes. In the present study we have used the exponential-power gap relation

$$k^{\mathrm{EP}}_{\ell\leftarrow 0}=\frac{\alpha_{10}}{[\ell(\ell+1)]^{c_{10}}}\exp\left(\frac{-b_{10}E_\ell}{kT}\right), \tag{10}$$

where α_{10}, b_{10}, and c_{10} are fitting constants.

Equations (7)–(10) do not include terms that could introduce preferences based on the parities of the initial and final rotational states. However, the energy transfer data for CO do show a tendency to preserve the parity when the amount of energy transferred is small. For the $X\,^1\Sigma^+$ state of CO, this tendency makes transfer events that cause even changes in J to be more probable than odd ΔJ transitions, when the energy gaps for the two processes are similar. From careful inspection of the full data set it was evident that the tendency to preserve the parity decayed with increasing amounts of transferred energy. The rate constant generating equations were modified to account for the parity preference by multiplying by the factor

$$p(J',J)=\left(1+\frac{a_{11}}{2}\sqrt{\frac{B_{v=2}}{\Delta E_{J'J}}}[1+(-1)^{J'+J+1}]\right)\times\left[1+b_{11}\exp\left(\frac{-c_{11}E(J')}{kT}\right)\right]. \tag{11}$$

This empirical expression was found by experimenting with various trial functions.

C. Computational simulations of the relaxation kinetics

Simulations of the RET data were made by numerical solution of Eq. (5) using a fourth-order Runge–Kutta method. To ensure that sufficient levels were considered in the model, all J levels in the range $J=0-29$ were included. The MEP, SPEG, and ECS-EP fitting law expressions were fitted to the family of $\bar{P}(J_i,J_f,x)$ curves by minimizing the variance between the predicted and observed population profiles. To facilitate calculation of the variance each $\bar{P}(J_i,J_f,x)$ curve was sampled at 100 points over the range from $x=0$ to 11.5.

For the first fitting cycle the rate constant expressions were used without the parity preference factor. The largest errors were associated with the populations in the initially excited levels $J_i=0$ and $J_i=14$ (for example, see the top trace in Fig. 7). As noted above, these errors originated from instrumental artifacts. Hence the population evolutions for the initially excited levels, and a few other curves that exhibited low signal-to-noise ratios, were removed from the fit. The scaling and fitting law parameters determined from the computer simulations, along with the literature values determined from pressure broadening studies of the Raman Q-branch spectrum, are listed in Table II. The estimated errors for each of the parameters were obtained by varying the parameter until a 10% increase in the variance was obtained while holding all other parameters constant.[43–45] The SPEG fitting law generated rotational transfer rate constants that best reproduced our data. The variance for the SPEG law was ~8% smaller than the best-fit variance of the MEG law. Surprisingly, the ECS-EP scaling law, which is derived from theoretical concepts, had the largest variance. However, the ECS-EP determined CO–CO interaction parameter (l_c) was a reasonable value of 6.4(±1.6) Å that is comparable to the 5.45(±65) Å value determined from Raman Q-branch pressure broadening coefficients.[12] The largest discrepancy between our parameters and the literature values (see Table II) occurs for the preexponential factor (α_7) of the SPEG law,

TABLE II. Comparison of the experimentally determined fitting parameters.

Parameters	Fitting results					
	MEG ($i=6$)		SPEG ($i=7$)		ECS-EP ($i=10$)	
$\alpha_i(10^{-11}$ cm^3 molecules^{-1} s$^{-1})$	6.62(32)[a]	10.00[b]	11.60(58)	48.67[c]	7.04(47)	7.71(12)[d]
b_i	1.430(42)	1.462	1.078(49)	1.295	0.076(24)	0.0543(21)
c_i	1.192(86)	1.246	0.228(11)	0.265	0.779(15)	0.7539(43)
l_c (Å)	[e]				6.4(1.6)	5.45(65)
σ^2 [f]	13.75		12.75		17.58	

[a]Experimental values form this work. Values in parenthesis are estimated error which were obtained by varying the parameter until a 10% increase in the variance was obtained while holding all other parameters constant.
[b]Experimental value, Ref. 13.
[c]Experimental value, Ref. 14.
[d]Experimental value, Ref. 12.
[e]Parameter not associated with the fitting law.
[f]Variance between experimental and computer simulated population evolutions.

which was determined previously by Looney *et al.*[14] The discrepancy in the α_7 value occurs because Looney *et al.*[14] restricted their relaxation model to allow only even ΔJ transitions, as this constraint improved the fit of their Raman Q-branch pressure broadening data.

Further calculations were performed to see if inclusion of the parity preference term could significantly improve the fits. The addition of the parity term greatly improved the SPEG fit, reducing the variance by more than ~45%. The greatest decrease in the average error per data point was for low J population evolutions. The parameters from the best-fit simulations are listed in Table III. The parity preference term also moderately improved the ECS-EP population evolutions, while it had minimal beneficial effects on the MEG law (compare the variance in Tables II and III). The parity weighted fit to the MEG model did not return statistically significant values of the fitting parameters of Eq. (11). The only parity parameter defined by the fit to the ECS-EP model was a_{11}.

The collision-dependent rotational level population evolutions for $J=0-18$ following excitation of the $J_i=0$, 7, and 14 levels are displayed in Figs. 8–10, respectively. In each of the figures the simulated populations are represented by the smooth curves through the raw data. These simulations were made using the SPEG model with inclusion of the parity preference term. To show the quality of the fit for levels with small equilibrium populations, the data in Figs. 8–10 are not all displayed on the same relative intensity scale. The agreement between the experimental data and the model was very favorable, with most of the simulations lying within the noise limits of the experimental data. One distinctive feature of the data was that the populations level off at about seven CO–CO hard sphere collisions as the $v=2$ manifold approached a Boltzmann distribution. The kinetic behavior in the range $x=0-7$ follows the pattern expected for relaxation to a thermal distribution. For excitation of $J_i=0$ the population moves upward, towards the 300 K Boltzmann maximum. As the energy gap dependence favors collisions that exchange small amounts of rotational energy, the higher J levels are populated by multicollision pathways.

As the $J=7$ level is at the maximum of the equilibrium population distribution, energy transfer following excitation of this level flows both to higher and lower J levels. This pattern is evident in Fig. 9. For this situation the population in the levels adjacent to $J_i=7$ increase smoothly, showing just the slightest hint of passing through a maximum near $x=2$.

Following the excitation of $J_i=14$ (see Fig. 10) a slight build up of population was observed in the adjacent levels at low collision numbers. The $J=14$ level lies above the

TABLE III. Experimentally determined parameters for the MEG, SPEG, and ECS-EP fitting and scaling laws with the addition of a parity preference factor.

Parameters	Fitting results		
	MEG[b] ($i=6$)	SPEF ($i=7$)	ECS-EP ($i=10$)
$\alpha_i(10^{-11}$ cm^3 molecules^{-1} s$^{-1})$	5.92(33)[a]	12.12(50)	7.32(39)
b_i	1.390(47)	1.046(34)	0.046(22)
c_i	1.114(72)	0.2629(90)	0.791(10)
l_c (Å)	[c]		4.4(1.7)
a_{11}	0.20(33)	−0.38(19)	−0.629(92)
b_{11}	0.20(21)	0.28(10)	0.14(16)
c_{11}	114(108)	4.7(2.0)	161(133)
σ^2 [d]	12.44	6.91	10.92

[a]Experimental values from this work. Values in parenthesis are estimated error which were obtained by varying the parameter until a 10% increase in the variance was obtained while holding all other parameters constant.
[b]Scaling and fitting laws with the addition of a parity preference factor.
[c]Parameter not associated with the fitting law.
[d]Variance between experimental and computer simulated population evolutions.

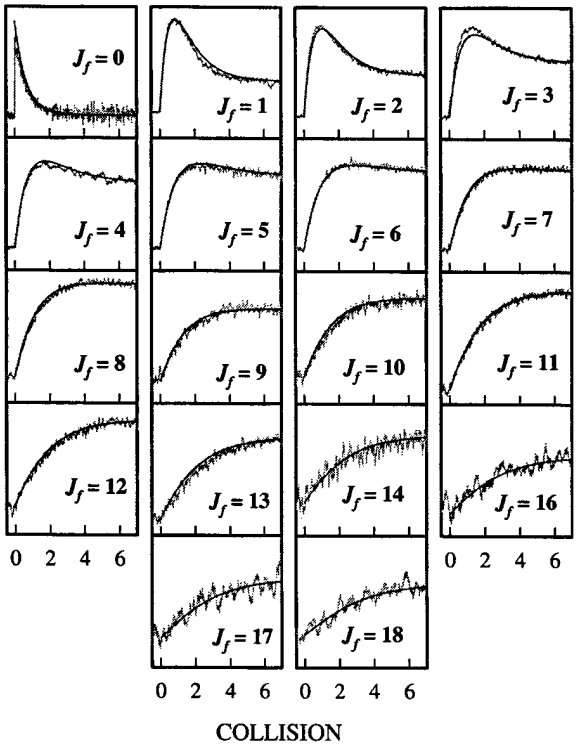

FIG. 8. The collision-dependent rotational population evolutions for $J_f=0-18$, with the exception of $J_f=15$, following the excitation of $J_i=0$. The computer simulated rotational populations are represented by the line through the experimentally determined rotational populations using the SPEG fitting law with the addition of the parity preference term.

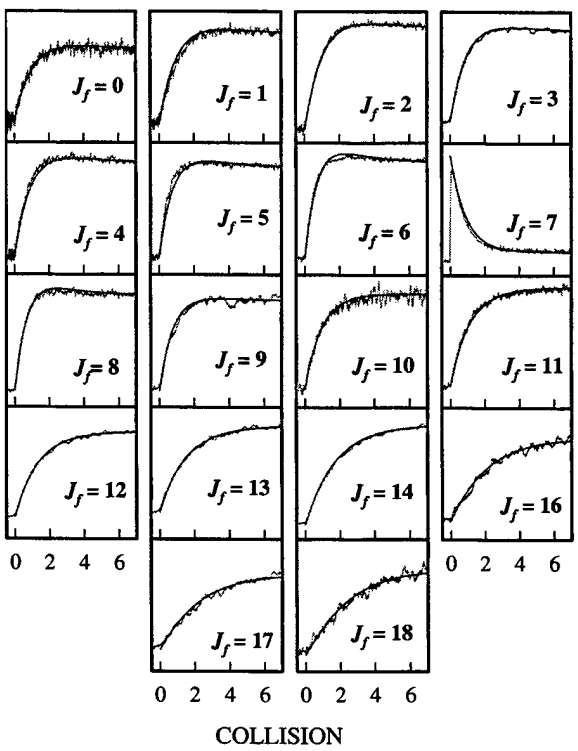

FIG. 9. The collision-dependent rotational population evolutions for $J_f=0-18$, with the exception of $J_f=15$, following the excitation of $J_i=7$. The computer simulated rotational populations are represented by the line through the experimentally determined rotational populations using the SPEG fitting law with the addition of the parity preference term.

Boltzmann maximum, such that it has an equilibrium population of ~3.8% of the total for $v=2$. Following excitation of $J=14$, 83.6% of the population must evolve to lower, and 12.6% must evolve to higher rotational levels. The energy gap between consecutive levels is quite large in the vicinity of $J=14$, so the fastest removal rates are those to the neighboring rotational levels. As these levels are still well above the Boltzmann maximum, their population profiles show maxima near $x=2$.

IV. DISCUSSION

The SPEG model, weighted for parity preferences, gave by far the best fit to the experimental data. To illustrate the magnitude of the parity selection term, Fig. 11(a) shows the differences between SPEG rate constants determined with and without the parity weighting. Note how the parity preference decays with increasing ΔJ. To compare the properties of the MEG, SPEG, and ESC-EP models it is helpful to examine the sets of rate constants that were determined without considering the parity weighting. Rate constant matrices for the three models are displayed graphically in Figs. 11(b)–11(d). The main defects of the best fit MEG model were that it underestimated the rate constants for small ΔJ transitions out of $J=0$, and the rate constants decreased too rapidly with increasing ΔJ [compare Figs. 11(b) and 11(d)]. The ECS-EP model generated rate constants for transfer out of the higher rotational levels that were too small. This defect can be seen by comparing Figs. 11(c) and 11(d).

All of the models predicted that multiquantum transfer collisions are important in CO–CO RET. This is not surprising as the rotational constant for CO ($B_{v=2}=1.888\ \mathrm{cm}^{-1}$)[46] is relatively small compared to kT at room temperature. Table IV shows the partitioning of the total removal rate constant over a range of $|\Delta J|$ values for the SPEG model with parity weighting. Here it can be seen that events with $|\Delta J|$ as high as 6 make an appreciable contribution to the RET kinetics. The last column in Table IV lists the total removal rate constant for each initial level. The rate constant for loss of population from $J=0$ is the largest and the rate constants fall slowly with increasing J over the range from $J_i=0$ to 12. In part, this gradual decrease occurs because the energy gaps surrounding the initial level increase linearly with J.

Consideration of the linewidth data recorded under low collision number conditions reveals an interesting correlation between the amount of rotational energy transferred and the associated effect on the inhomogeneous linewidth of the probe transition. Plots of the linewidth data, such as those shown in Fig. 5, can be extrapolated back to the y-axis intercept to obtain the single collision linewidth limit. Initial linewidths for levels populated by transfer from $J_i=0$ are given in Table V. When these data are correlated with the $k_{J\leftarrow 0}$ rate constants it is apparent that the smallest linewidths are associated with the largest rate constants. This trend is consistent with a classical model of the RET dynamics. Large rate constants occur when the transfer process can be induced by collisions that have large impact parameters. Since it is the

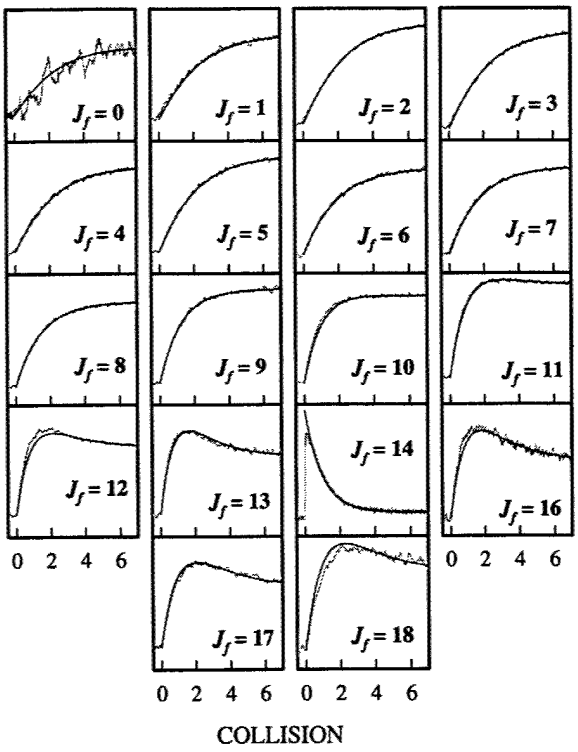

FIG. 10. The collision-dependent rotational population evolutions for $J_f = 0-18$, with the exception of $J_f = 15$, following the excitation of $J_i = 14$. The computer simulated rotational populations are represented by the line through the experimentally determined rotational populations using the SPEG fitting law with the addition of the parity preference term.

long-range region of the CO–CO interaction potential that is sampled by these collisions the forces acting between the collision pairs are weak, so the amount of rotational energy that can be transferred is small (this is one of the factors responsible for the energy gap dependence of the rate constants). As these weak collisions are not very effective in reorienting the velocity vectors, rotational transfer occurs without much change in the linewidth of the probe transition (as compared to the linewidth of the velocity distribution created by the excitation laser). Conversely, small impact parameter (hard) collisions are needed to transfer larger quantities of rotational energy. These events sample the repulsive wall of the intermolecular potential, where the intermolecular forces are relatively strong. The smaller cross sections for these events lead to smaller rate constants while the hard collisions are effective in reorienting the velocities and thereby broadening the initial linewidth of the probe transition.

This simple picture of the collision dynamics can also account for the behavior of the parity preference when the general details of the intermolecular potential energy surface are considered. To understand the origin of the parity preference it is convenient to consider an atom–rigid diatom model and expand the intermolecular potential in terms of Legendre polynomials. Jacobi coordinates are used for this expansion, where R is the distance between the centers of mass of the colliding pair and θ is the angle between R and the C–O bond axis of the target molecule. The effective intermolecular potential can then be expressed by the equation

$$V(R,\theta) = \sum_{\ell} C_{\ell}(R) P_{\ell}(\cos\theta), \tag{12}$$

where the $C_{\ell}(R)$ functions are radially dependent expansion coefficients and the $P_{\ell}(\cos\theta)$ term are Legendre polynomials. The even-ℓ terms in this expansion do not mix the parity states of the target CO, so they can only mediate transfer between levels of the same parity (even ΔJ transitions). The odd-ℓ terms mix states of opposite parity, mediating odd ΔJ transfer. As the charge distribution of the CO molecule is fairly symmetric, the expansion of the long-range region of the intermolecular potential is dominated by even-ℓ terms. Hence the large impact parameters events (small amount of rotational energy transferred, with little change in the linewidth) have the greatest tendency to conserve the parity. At short range the repulsive wall of the potential shows significant differences for the two ends of the molecule, so this part of the potential is represented by both even and odd terms in Eq. (12). Consequently hard collisions are less likely to conserve the parity. The data for transfer from $J_i = 0$ to the J

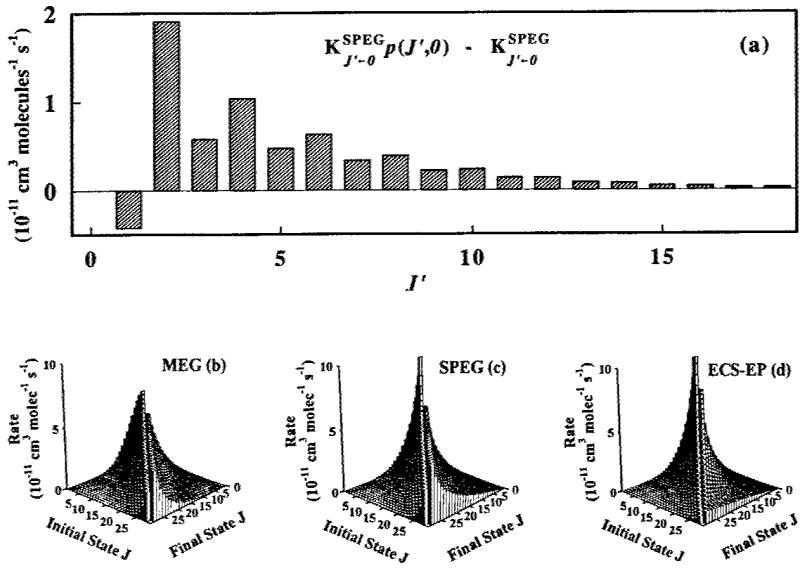

FIG. 11. (a) A bar graph that illustrates the difference between SPEG rate constants determined with and without the parity weighting. Three-dimensional plots of the best fit rate constant matrices generated from the MEG, SPEG, and ESC-EP models are displayed graphically in (b)–(d).

TABLE IV. Percent fractional contribution of single and multiple quantum state transitions which remove population from the initial state J.

Inital J	Percent fractional removal rate												Total removal rate
	$\|\Delta J\|=1$	2	3	4	5	6	7	8	9	10	11	12	
0	17.74	17.48	12.24	11.13	8.45	7.41	5.69	4.81	3.66	2.98	2.22	1.75	52.3[a]
1	24.52	16.25	11.73	10.42	7.94	6.82	5.21	4.32	3.25	2.60	1.91	1.47	46.5
2	28.83	19.34	10.81	9.39	7.12	5.99	4.53	3.69	2.74	2.15	1.56	1.18	43.2
3	29.84	22.47	12.46	8.44	6.34	5.23	3.90	3.11	2.28	1.75	1.25	0.93	40.5
4	29.74	23.29	14.72	9.60	5.62	4.54	3.35	2.62	1.89	1.42	1.00	0.73	38.3
5	29.16	23.16	15.61	11.47	6.43	3.95	2.86	2.19	1.56	1.15	0.80	0.57	36.6
6	28.40	22.60	15.77	12.27	7.89	4.67	2.45	1.84	1.28	0.93	0.63	0.44	35.4
7	27.62	21.86	15.54	12.45	8.63	6.01	3.06	1.55	1.06	0.76	0.50	0.35	34.6
8	26.87	21.10	15.14	12.30	8.90	6.73	4.20	2.15	0.88	0.61	0.40	0.27	34.0
9	26.18	20.38	14.67	11.98	8.89	7.04	4.87	3.22	1.41	0.50	0.32	0.21	33.7
10	25.52	19.70	14.21	11.61	8.74	7.10	5.21	3.88	2.35	1.02	0.26	0.17	33.5
11	24.89	19.06	13.76	11.24	8.54	7.04	5.35	4.25	2.96	1.89	0.71	0.13	33.5
12	24.27	18.46	13.34	10.89	8.33	6.92	5.38	4.43	3.33	2.48	1.48	0.56	33.5
13	23.66	17.88	12.93	10.56	8.13	6.80	5.37	4.52	3.54	2.85	2.01	1.27	33.6
14	23.06	17.32	12.55	10.26	7.94	6.68	5.33	4.55	3.66	3.07	2.36	1.77	33.7
15	22.48	16.78	12.17	9.96	7.76	6.57	5.30	4.57	3.73	3.21	2.58	2.10	33.8
16	21.92	16.27	11.81	9.68	7.59	6.47	5.27	4.58	3.79	3.31	2.73	2.32	34.0
17	21.38	15.78	11.47	9.42	7.43	6.37	5.23	4.58	3.83	3.38	2.83	2.47	34.1
18	20.86	15.32	11.14	9.16	7.27	6.27	5.20	4.59	3.87	3.44	2.92	2.55	34.3
19	20.37	14.88	10.83	8.92	7.12	6.18	5.16	4.58	3.91	3.49	2.95	2.64	34.5
20	19.90	14.47	10.54	8.70	6.98	6.08	5.12	4.58	3.93	3.49	3.02	2.72	34.6
21	19.47	14.08	10.27	8.49	6.84	5.99	5.07	4.56	3.87	3.53	3.08	2.79	34.8
22	19.06	13.72	10.01	8.29	6.72	5.91	5.03	4.42	3.89	3.57	3.13	2.85	34.9
23	18.68	13.39	9.78	8.11	6.60	5.83	4.80	4.42	3.91	3.59	3.17	2.90	35.0
24	18.35	13.10	9.57	7.95	6.50	5.44	4.79	4.42	3.92	3.62	3.21	2.95	35.1
25	18.06	12.84	9.40	7.82	5.89	5.42	4.78	4.42	3.93	3.64	3.24	2.99	35.0
26	17.86	12.65	9.27	6.79	5.89	5.42	4.79	4.44	3.96	3.67	3.28	3.03	34.9
27	17.80	12.56	7.55	6.82	5.92	5.46	4.83	4.48	4.00	3.72	3.33	3.09	34.5
28	18.02	9.34	7.70	6.96	6.05	5.58	4.95	4.59	4.11	3.82	3.43	3.19	33.5
29	11.86	9.85	8.13	7.35	6.40	5.90	5.24	4.86	4.36	4.06	3.65	3.40	31.5

[a]Units of (10^{-11} cm^3 molecules^{-1} s^{-1}) determined for the best-fit of data using the SPEG law and a parity preference factor.

$=1$ and 2 levels supports this view of the dynamics. The initial linewidth for $J=1$ is greater than that for $J=2$, despite the larger energy gap for $\Delta J=2$ transfer (cf. Table V). This situation occurs because the $\Delta J=1$ transfer requires collisions that sample the asymmetric region of the potential.

TABLE V. Initial linewidths for levels populated by collisions from $J_i=0$ and 7.

J_f	$\Delta\nu(J_i=0)$[a]	$\Delta\nu(J_i=7)$
0	74	135
1	115	121
2	91	116
3	109	118
4	113	126
5	117	121
6	112	125
7	111	71
8	122	122
10	120	116
11	128	127
12	131	131
13	137	127
14	143	142
16	144	141
17	143	140
18	143	143

[a]MHz units.

The question of whether it is energy transfer or angular momentum transfer that governs RET has been examined by previous investigators.[47,48] For atom–diatom collisions, models have been proposed that predict that it is angular momentum transfer that determines the probabilities. In the present study the linewidth data provides some insight concerning the factor that is most important in CO–CO RET. The initial linewidths for levels populated by transfer out of $J_i=7$ may be compared with the corresponding linewidths for $J_i=0$ in Table V. The overall trend is that the linewidths for levels populated from $J_i=0$ are narrower than those for levels populated from $J_i=7$ when transitions with the same value of ΔJ are compared. While the amount of angular momentum is defined by ΔJ the energy transfer is dependent on ΔJ and J_i. The larger linewidths for transfer out of $J_i=7$ are consistent with the dynamical model presented above, and indicative of transfer governed by the energy gaps.

V. SUMMARY

IR double resonance techniques were used to examine rotational energy transfer and velocity redistribution in CO–CO collisions. These measurements involved pulsed excitation of a single J level and time-resolved cw spectroscopic probing of the initially excited level and levels close

enough in energy to be populated by collisional transfer. Time-dependent rotational populations were characterized for 54 pairs of initial and final rotational states. The RET data were analyzed by numerically solving the master equation. Scaling and fitting laws were used to generate the rate constants for the master equation. Three types of fitting law expressions were investigated: MEG, SPEG, and ECS-EP. The best results were obtained using the SPEG model. Transfer events that involved small changes in the rotational energy showed a preference for even-ΔJ transitions, which preserve the parity of the target molecule. The SPEG equation, multiplied by an empirical function to take parity weighting into account, gave excellent agreement with the experimental data.

The probe transition linewidths of the collisionally populated levels were also examined in this study. For conditions that were effectively single collision we observed a correlation between the inhomogeneous linewidths and the corresponding state-to-state transfer rate constants. In essence, the linewidths decreased as the rate constants increased. This behavior was interpreted in terms of a simple classical mechanics model. The large rate constants correspond to processes mediated by long-range interactions that have little effect on the velocity distribution (minimal inhomogeneous line broadening), whereas small rate constants are associated with hard collisions that reorient the velocity vectors. The classical model was also consistent with the observation that the tendency to preserve the parity (which favors ΔJ-even transfer) was lost as the amount of rotational energy exchange increased. This behavior was seen because soft collisions sample the near-symmetric long-range region of the intermolecular potential, while hard collisions rebound from the asymmetric repulsive wall.

This study is the first to provide sufficient state-to-state rate constant data for a critical evaluation of the scaling and fitting law models as they apply to CO–CO collisions. In addition to providing a detailed picture of CO RET dynamics, the results reported here will be of value for future studies of the kinetics of discharge and optically pumped CO lasers.

ACKNOWLEDGMENTS

T.C.S. would like to thank the National Research Council for a postdoctoral fellowship. This work was supported by the Air Force Office of Scientific Research (AFOSR). M.C.H. thanks the AFOSR for support of this work through Grant No. AFOSR F49620-01-1-0070.

[1] G. Ganzi and S. I. Sandler, J. Chem. Phys. **55**, 132 (1971).
[2] A. Das Gupta and T. S. Storvick, J. Chem. Phys. **52**, 742 (1970).
[3] A. P. Malinauskas, J. W. Gooch, B. K. Annis, and R. E. Fuson, J. Chem. Phys. **53**, 1317 (1970).
[4] R. Fei, H. M. Lambert, T. Carrington, S. V. Filseth, C. M. Sadowski, and C. H. Dugan, J. Chem. Phys. **100**, 1190 (1994).
[5] R. Fei, D. E. Adelman, T. Carrington, C. H. Dugan, and S. V. Filseth, Chem. Phys. Lett. **232**, 547 (1995).
[6] R. J. Hall, IEEE J. Quantum Electron. **QE-12**, 453 (1976).
[7] L. H. Sentman, J. Chem. Phys. **67**, 966 (1977).
[8] J. J. T. Hough and R. L. Kerber, Appl. Opt. **14**, 2960 (1975).
[9] A. Ben-Shaul, K. L. Kompa, and U. Schmailzl, J. Chem. Phys. **65**, 1711 (1976).
[10] J. G. Skifstad and C. M. Chao, Appl. Opt. **14**, 1713 (1975).
[11] J. R. Creighton, IEEE J. Quantum Electron. **QE-11**, 699 (1975).
[12] G. Millot, J. Chem. Phys. **93**, 8001 (1990).
[13] G. J. Rosasco, L. A. Rahn, W. S. Hurst, R. E. Palmer, and S. M. Dohne, J. Chem. Phys. **90**, 4059 (1989).
[14] J. P. Looney, G. J. Rosasco, L. A. Rahn, W. S. Hurst, and J. W. Hahn, Chem. Phys. Lett. **161**, 232 (1989).
[15] B. Dill and H. Heydtmann, Chem. Phys. **35**, 161 (1978).
[16] R. G. MacDonald and J. J. Sloan, Chem. Phys. **40**, 321 (1979).
[17] K. Tamagake, D. W. Setser, and J. P. Sung, J. Chem. Phys. **73**, 2203 (1980).
[18] Z. B. Alfassi and M. Baer, IEEE J. Quantum Electron. **QE-15**, 240 (1979).
[19] R. L. Kerber, R. C. Brown, and K. A. Emery, Appl. Opt. **19**, 293 (1980).
[20] J. E. McCord, H. C. Miller, G. D. Hager, A. I. Lampson, and P. G. Crowell, IEEE J. Quantum Electron. **35**, 1602 (1999).
[21] J. E. McCord, A. A. Ionin, S. P. Phipps, P. G. Crowell, A. I. Lampson, J. K. McIver, A. J. W. Brown, and G. D. Hager, IEEE J. Quantum Electron. **36**, 1041 (2000).
[22] M. P. Saksena, P. Tondon, and S. Saxena, Indian J. Pure Appl. Phys. **7**, 79 (1969).
[23] H. J. Bauer and H. Kosche, Acustica **17**, 96 (1966).
[24] P. G. Kistemaker, A. Tom, and A. E. De Vries, Physica **48**, 414 (1970).
[25] G. J. Prangsma, A. H. Alberga, and J. J. M. Beenakker, Physica **64**, 278 (1973).
[26] A. E. Belikov, Mol. Phys. **98**, 343 (2000).
[27] D. Bassi, A. Boschetti, S. Marchetti, G. Scoles, and M. Zen, J. Chem. Phys. **74**, 2221 (1981).
[28] M. M. Ahern, D. A. Steinhurst, and M. A. Smith, Chem. Phys. Lett. **300**, 681 (1999).
[29] A. E. Belikov, M. L. Strekalov, and A. V. Storozhev, Chem. Phys. Lett. **304**, 253 (1999).
[30] R. G. Sharafutdinov, A. E. Belikov, M. L. Strekalov, and A. V. Storozhev, Chem. Phys. **207**, 193 (1996).
[31] J. J. BelBruno, J. Gelfand, and H. Rabtiz, J. Chem. Phys. **78**, 3990 (1983).
[32] P. Brechignac, Opt. Commun. **25**, 53 (1978).
[33] P. Brechingac, A. Picard-Bersellini, and R. Charneau, J. Phys. B **13**, 135 (1980).
[34] M. L. Koszkowski, L. A. Rahn, R. E. Palmer, and M. E. Coltrib, J. Phys. Chem. **91**, 41 (1987).
[35] T. A. Brunner and D. Pritchard, Adv. Chem. Phys. **50**, 589 (1982).
[36] B. C. Sanctuary, Chem. Phys. Lett. **62**, 378 (1979).
[37] T. A. Brunner and D. Pritchard, in *Dynamics of the Excited State*, edited by K. P. Lawely (Wiley, New York, 1982), p. 589.
[38] A. E. DePristo, S. D. Augustin, R. Ramaswamy, and H. Rabitz, J. Chem. Phys. **71**, 850 (1979).
[39] J. O. Hirschfelder, C. F. Curtiss, and R. B. Bird, *Molecular Theory of Gases and Liquids* (Wiley, New York, 1954).
[40] K. P. Huber and G. Herzburg, *Molecular Spectra and Molecular Structure-IV: Constants of Diatomic Molecules* (Van Nostrand Reinhold, New York, 1979).
[41] G. D. Billing, in *Nonequalibrium Vibrational Kinetics*, edited by M. Capitelli (Springer Verlag, Berlin, 1986).
[42] A. R. Edmonds, *Angular Momentum in Quantum Mechanics* (Princeton University Press, New Jersey, 1985), p. 49.
[43] F. Menard-Bourcin, T. Delaporte, and J. Menard, J. Chem. Phys. **84**, 201 (1986).
[44] R. A. Copeland and F. F. Crim, J. Chem. Phys. **78**, 5551 (1983).
[45] J. J. Hinchen and R. H. Hobbs, J. Appl. Phys. **50**, 628 (1979).
[46] G. Herzburg, *Molecular Spectra and Molecular Structure-I: Spectra of Diatomic Moleculesc Molecules* (Van Nostrand Reinhold, New York, 1950), p. 522.
[47] A. J. McCaffery, Z. T. Alwahabi, M. A. Osborne, and C. J. Williams, J. Chem. Phys. **98**, 4586 (1993).
[48] M. Osborne and A. J. McCaffery, J. Chem. Phys. **101**, 5604 (1994).